Central uplift collapse in acoustically fluidized granular targets: Insights from analog modeling

M. A. DÖRFLER ⓘD* and T. KENKMANN ⓘD

Institut für Geo- und Umweltnaturwissenschaften, Geologie, Albert-Ludwigs-Universität Freiburg, Albertstrasse 23-B,
79104 Freiburg, Germany
*Corresponding author. Email: matthias.doerfler@neptun.uni-freiburg.de

Abstract–Depending on their sizes, impact craters have either simple or complex geometries. Peak-ring craters such as the Chicxulub impact structure possess a single interior ring of peaks and hills and a flat interior floor. The exact mechanisms leading to the formation of a morphological peak-ring are still a matter of debate. In this study, analog modeling was used to study the flow field of a collapsing central uplift. A 3-D-printed cast was used to bring the analog material in the shape of an overheightened central uplift that was based on numerical modeling. The cast was then quickly removed and the central peak collapsed, forming a flattened broad mound that spread out onto the annular moat of the crater cavity. A subwoofer was used to fluidize the granular target material. The kinematics of the collapse were analyzed with the aid of particle image velocimetry, revealing a downward and outward collapse of the central uplift. This mode of collapse is partly in agreement with numerical models, in particular for the initial and middle phases. The overthrusting of the collapsing central peak onto the inward moving crater floor predicted by numerical modeling was observed, though to a lesser degree. A peak-ring, however, could not be reproduced since the collapse came to a halt before the central peak was completely leveled. Nevertheless, the method provides qualitative insights into the kinematics of collapse phenomena. This experimental study provides independent support of the theory of acoustic fluidization, in addition to numerical simulations.

INTRODUCTION

Peak-ring craters are an important class of large-scale complex impact structures in the solar system. They are known from the Earth (Morgan et al. 2016), the Moon (Baker et al. 2011a), Mars (Barlow and Bradley 1990), Venus (Phillips et al. 1991), Mercury (Baker et al. 2011b), but not from icy satellites and asteroids. On Earth, Chicxulub is the only terrestrial impact crater confirmed to possess an unequivocal peak-ring. Investigating the internal structure of the peak-ring of the Chicxulub impact structure was one of the main objectives of the recent IODP-ICDP Expedition 364 (Morgan et al. 2016). Peak-ring craters have a terraced rim, a flat floor, and a single interior ring of peaks with a diameter of about half of the final crater diameter (Fig. 1; Baker et al. 2016). Explanations as to how peak-rings form are offered by several different models. Of these, the "conceptual geological model" (Head 2010; Baker et al. 2016) and the "numerical model" (Collins et al. 2002) are currently most popular. In both models, peak-ring formation is attributed to the modification stage of cratering. In the conceptual geological model, the vertical translation of the central uplift leads to a rotational movement of the inward collapsing cavity walls, resulting in an upward component in their movement. The peak-ring is then formed in a zone of convergence of the inward collapsing cavity walls and the central uplift. One important aspect of this model is that no prominent central peak develops due to a larger amount of impact melt, which is unable to support the steep topography of a central uplift. Numerical models (e.g., Collins et al. 2002) predict that a central uplift forms, which then exceeds gravitational stability. This overheightened central
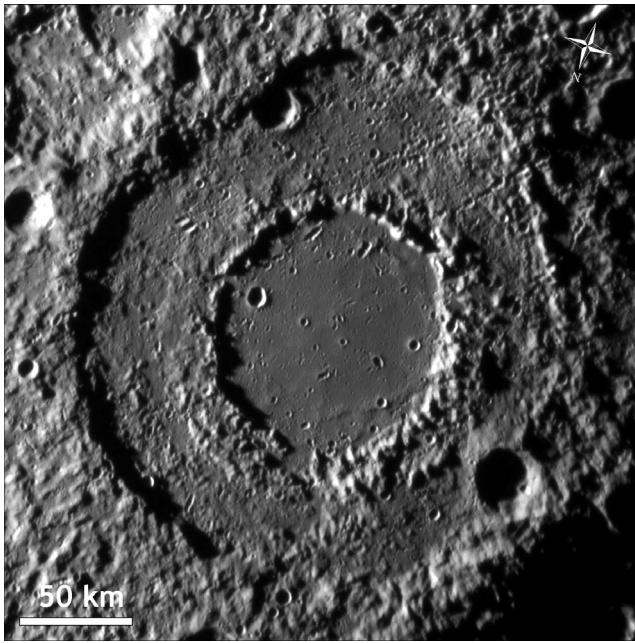
Fig. 1. Peak-ring crater Michelangelo on Mercury. Source: Messenger, Mercury Dual Imaging System (MDIS).

peak then collapses downward and outward, overthrusting the previously collapsed cavity walls, which eventually forms the peak-ring. Numerical simulations of impact cratering successfully reproduce the morphology of the Chicxulub impact structure (Morgan et al. 2016) and planetary peak-ring craters in general. Also, results from the IODP-ICDP Expedition 364 (Christeson et al. 2018) are consistent with the numerical model: the presence of uplifted shocked rocks in the peak-ring as predicted by numerical simulations could be confirmed and the movements of the involved rocks could be reconstructed based on successive rotations of shock indicators and the timing of deformation events (Morgan et al. 2016; Riller et al. 2018; Rae et al. 2019a, 2019b). Moreover, the important role of a temporary strength degradation could be demonstrated during uplift and collapse of the central peak. The transition from distributed cataclastic flow to localized shear-faulting and the progressive increase in fault spacing was interpreted as the waning of this temporary weakening that resulted in the target regaining sufficient strength to support the topography of the peak-ring (Riller et al. 2018).

Melosh (1977) proposed that a mechanism, known as "acoustic fluidization," could explain the temporary weakening of rocks during crater formation. Here, we investigate the role of acoustic fluidization from an experimental perspective. For this, we use techniques of analog modeling applied to granular media.

Acoustic Fluidization

The yielding of rocks by brittle deformation is commonly described using the Mohr–Coulomb failure criterion:

$$\tau = C + \sigma_n \tan \Phi \tag{1}$$

where τ is the shear strength (Pa), σ_n the normal stress (Pa), C is the cohesion (Pa), and Φ the angle of internal friction (°). Melosh (1977) and McKinnon (1978) demonstrated that the rock masses involved in crater formation need to have a drastically reduced cohesion of about 3 MPa and almost no internal friction for an uplift of the crater floor, and therefore the formation of complex craters, to occur. O'Keefe and Ahrens (1993, 1999) proposed a dry friction reduction via thermal softening and extensive rock damage as a weakening mechanism. However, the volume of rocks that gets sufficiently hot during impact cratering is not large enough (Kenkmann et al. 2013). Therefore, the most widely accepted weakening mechanism is the concept of acoustic fluidization. In the original model proposed by Melosh (1979), elastic waves traveling through the rock debris in the wake of the shock cause pressure fluctuations which periodically reduce the overburden pressure of the overlying material. This momentary reduction of normal stress effectively lowers the material's strength, allowing slip events to take place and resulting in a bulk behavior of the material as a viscous fluid. This original model, however, is a continuum model in which the wavelength of the elastic waves has to be assumed and is not constrained by observations in nature. Ivanov and Kostuchenko (1997) developed the block oscillation model, based on observations from drillings into the Puchezh-Katunki impact structure, where discrete blocks of several hundred meters size separated by thinner interbreccia layers were observed (Ivanov et al. 1996). In this model, the oscillation of individual blocks periodically reduces the frictional forces between them, allowing them to move, resulting in a Bingham fluid-like behavior with a yield strength Y (Melosh and Ivanov 1999). The effective viscosity η in this model is given by

$$\eta = \frac{2\pi h^2 \rho}{T} \tag{2}$$

where the oscillation period T is proportional to the characteristic block size h:

$$T = \frac{2\pi h}{c_b} \sqrt{\frac{\rho h_b}{\rho_b h}} \tag{3}$$

Table 1. Model to natural scaling parameters.

	Density ρ (kg m^{-3})	Length L (m)	Gravity g (m s^{-2})	Time t (s)	Viscosity η (Pas)
Analog model	1550	0.103	9.81	0.76	50
Nature	2900	60,400	9.81	60	4E+09[b]
Ratio model/nature	5.3E-01	1.7E-06	1.0E+00	1.3E-02	1.2E-08[a]

The model-to-nature ratio of the viscosity indicated with "a" is calculated using Equation 5. The viscosity of acoustically fluidized rock in nature, indicated with "b" is calculated from the viscosity measured in the analog model and the calculated viscosity ratio.

In this model, the sound velocity, density, and thickness of the interbreccia layer are c_b, ρ_b, and h_b, respectively, and ρ the density of the blocks (Ivanov and Artemieva 2002). Most numerical simulations make use of this block oscillation model to implement acoustic fluidization, enabling them to accurately reproduce the crater morphologies observed in nature. They assign a constant effective viscosity and a time-dependent yield strength, resulting in a time-varying Bingham fluid rheology (e.g., Collins et al. 2002; Ivanov and Artemieva 2002; Rae et al. 2016). The duration for which the fluidization remains active is determined by a decay constant (Wünnemann and Ivanov 2003). A parameter study by Martellato and Wünnemann (2018) has shown that the decay time is the parameter responsible for the largest variations in the final crater morphometry (e.g., diameter and depth), and whether or not a central uplift develops. While so far no proof for acoustic fluidization was found in the field, some observations of oscillating, multidirectional fault motions are in accordance with it (Kenkmann et al. 2000) and deformation observed in the Chicxulub target rock support the theory as well (Riller et al. 2018).

Analog Modeling and Particle Image Velocimetry

In analog experiments, granular materials such as sand or glass beads are used to mimic the discontinuous deformation of geological materials on a laboratory scale. These types of experiments are a well-established geoscientific method used to investigate the kinematics of a variety of geological deformation processes such as the formation of orogenic wedges and landslides (e.g., Davis et al. 1983; Schellart and Strak 2016). Analog modeling was also applied for impact crater studies, for example, Kenkmann et al. (2007), Riller et al. (2010), Kenkmann and Burgert (2011), Aschauer and Kenkmann (2017). In order for the model to accurately mimic a natural process, a proper scaling with respect to length, cohesion, and gravity is crucial. The dimensionless scaling factor for brittle deformation S_b of these experiments is given by

$$S_b = \frac{C_n \rho_m a}{C_m \rho_n g} \qquad (4)$$

where C is the cohesion (Pa), ρ the density (kg/m^3), and g and a are the gravity (m s^{-2}) in nature and the

laboratory, respectively (Hoth 2005). The subscripts m and n stand for model and nature. Analog models involving viscous materials such as acoustically stimulated materials also require a scaling of time, viscosity, and strain rate/velocity. Neglecting the effect of inertial forces, and assuming Newtonian viscosities, dynamic similarity between nature and model leads to the following scaling of time (Childs et al. 1993):

$$t_R = \frac{1}{\dot{e}_R} = \frac{\eta_R}{\rho_R g_R L_R} \qquad (5)$$

where the subscript R denotes the ratio between analog and nature of the quantities time t, strain rate $\dot{e}$, viscosity η, density ρ, gravity g, and length L. Table 1 gives a summary of the scaling parameters and their respective ratios applicable to our experiments: the ratios of density, gravity, length, and timeframe are known, which we use to calculate the ratio between viscosities in model and nature, applying Equation 5. Using the viscosity of the fluidized granular material, we can then calculate the corresponding viscosity in nature. These scaling relationships use static measurements; we note that the viscosity is subject to variations during dynamic deformation. Thus, the derived viscosity is a representative viscosity of the material. Crater collapse in nature also occurs under varying viscosities. Velocities and strain can be derived from particle image velocimetry (PIV), which traces the movement of the granular particles. The movement is recorded with cameras and the obtained footage is analyzed with computer programs using image-cross-correlation algorithms (Grant 1997). This method allows us to quantitatively evaluate the analog experiments.

For this study, a new approach toward the analog modeling of impact crater formation was developed. Instead of using an air gun to produce a small-scale impact from the beginning to the end of the cratering process (Aschauer and Kenkmann 2017; Martellato et al. 2018), the experiment starts in the middle of the modification stage to enable a more detailed investigation of the processes taking place during that stage. To achieve this, a 3-D-printed negative of an overheightened central uplift was used to keep the granular material (glass beads) in place until it was

suddenly released when the experiment was initiated. Throughout the collapse, the material was fluidized by vibration. Since this method of achieving fluidization in analog experiments investigating complex crater formation is new, we provide a comprehensive overview of previous works on granular flow and fluidization of granular materials.

Fluidization of Granular Media

In terms of their bulk mechanical behavior, granular materials are generally described by three material properties: the cohesion C (Pa), the angle of internal friction Φ (°), and the angle of repose α_r (°), where $\alpha_r < \Phi$ (Jaeger et al. 1990; Campbell 2005). The stability of granular slopes follows the Mohr–Coulomb failure criterion (Equation 1) as well (Campbell 2005). On the grain scale, the material strength is governed by intergrain contacts and dry friction (Jaeger et al. 1990). External forces applied to a granular material create force chains or networks of grains in contact, distributing the load. Another factor influencing the bulk properties of a granular material is the coordination number/packing configuration of the grains, with a higher coordination number resulting in a stiffer, more resilient material (Campbell 2005). An avalanche in a granular slope is triggered either when the material's yield strength is exceeded or by external perturbations such as vibrations or shocks when the slope angle is in the metastable field between α_r and Φ (Jaeger et al. 1990). The failure in granular materials occurs along narrow shear bands, following the Mohr–Coulomb law (Campbell 2005). Therefore, avalanches are restricted to a surface layer below which no motion occurs. At low shear rates, this granular flow is governed by dry friction between the grains. However, this intergrain friction decreases rapidly with increasing shear rate since the dilation reduces the time individual grains are in contact with each other (Jaeger et al. 1990). Furthermore, at high shear rates, the formation of force chains is hindered by the reduced grain contact time, effectively promoting granular flow (Campbell 2005). Nichol and Van Hecke (2012) studied the shear-induced fluidization of glass beads. They observed that a shear applied to a granular material produces non-local fluidization of the whole material which then shows no yield strength and follows Archimedes law. They were able to assign an effective viscosity to the material, noting that it is inversely proportional to the shear rate and increases with the filling height of the granular material in the test container. The effect of vibrations on granular material has been investigated in several studies. The amount of vibrational energy supplied to the system is given by the dimensionless parameter Γ:

$$\Gamma = A(2\pi)^2/g \qquad (6)$$

where A is the amplitude (m), f the frequency (Hz), and g the gravitational acceleration (m s^{-2}; Wortel et al. 2014), or variations of this term used by some authors. Wortel et al. (2014) subjected glass beads to vertical vibrations with a frequency of 63 Hz and investigated the rheology of this material. They observed a compaction of the material for weak vibrations and fluidization for strong vibrations. Similar to Nichol and Van Hecke (2012), they found that increasing the filling height increased the viscosity, and increasing vibrational energy reduced it. Rubin et al. (2006) subjected inclined beds of glass beads to horizontal vibrations. They note that weak vibrations cause the packing configuration of the grains to evolve with time and a rearrangement and reinforcement of the force network, both leading to an increased slope stability. In their experiments with glass beads, vibrations could simultaneously cause compaction and strengthening alongside a fluidization of the material. Marchal et al. (2013) stated that low shear acts to stabilize the force network, while high shear or external perturbations like vibrations destabilize it. They conclude that a higher frequency or amplitude decrease the viscosity of granular material, with the vibrational energy, Γ, being the only controlling parameter. Swisher and Utter (2014), however, observed that high frequencies had a stabilizing effect, allowing the grains to settle into more stable configurations, whereas a higher amplitude destabilized the material, although they note that this effect might be enhanced by the irregular shaped grains they used.

To summarize, the flow of granular materials fluidized by vibrations is a highly complex phenomenon, in which a multitude of parameters influences the behavior of the material. Vibrations cause competing effects, on the one hand, fluidizing the material via dry friction reduction, while at the same time compacting and thereby strengthening the granular material. In vibration, a granular material exhibits fluid-like behavior, which allows us to characterize it by measuring its effective viscosity. This viscosity decreases with shear rate and higher vibrational energy and increases with material depth.

MATERIALS AND METHODS

The analog materials used were glass beads of three different grain sizes. These materials have been successfully employed in previous experiments (Aschauer and Kenkmann 2017) and are suitable for this study since their low cohesion and internal friction

Table 2. Material properties of glass beads used for the experiments (see also Aschauer and Kenkmann 2017): grain size d_g, bulk density ρ_b, angle of repose α_r, angle of internal friction Φ, and the cohesion C. The intermediate glass beads actually have a diameter of 250–420 μm, but data on their properties were unavailable, so the values of a comparable grain size* are given instead from Burgert (2011).

d_g (μm)	ρ_b (kg m^{-3})	α_r (°)	Φ (°)	C (Pa)
420–840	1.55 ± 0.001	25.8 ± 0.2	28.3 ± 0.2	57.3 ± 60.2
300–400*	1.64 ± 0.060	–	25.89 ± 0.17	63.3 ± 16
150–250	1.48 ± 0.011	23.2 ± 0.2	24.1 ± 0.1	3.0 ± 21.7

make them easier to fluidize. Their properties are presented in Table 2. The scaling relationships are summarized in Table 1. The viscosity of the acoustically fluidized rock in nature was obtained by applying Equation 5 (Table 1). The analog model values are constants, measured statically (see Table 2), while "natural" values vary widely in the process of cratering.

A core element of this study was a cast of the developing Chicxulub crater. It is based on a snapshot of a numerical simulation of the crater formation during the highest extent of the central uplift. The data for this were provided by Gareth Collins (Imperial College) from an unpublished simulation (Fig. 2), but it does not differ greatly from already published simulations (Morgan et al. 2016). Using CAD software, this simple profile was turned into a radially symmetric, three-dimensional cross section by rotating it 180° around the y-axis. This was then printed out with a 3-D printer as a negative cast of the crater. The cast has a scale of $1:586,400 \pm 6000$ (Table 1).

Next, a box to hold the granular analog material was designed around the cast. The dimensions match exactly those of the cast so that the cast simply rests on the walls acting as a lid. The front wall is a Plexiglass pane, allowing us to observe the flow of the granular material. An aluminum plate at the bottom can be removed to open up the filling-hatch. This allows us to completely fill out the shape of the cast by turning the box upside down, with the lid held in place by two straps.

An integral part of the experimental setup is the acoustic excitation of the granular media in order to simulate the phenomenon of acoustic fluidization. We installed a subwoofer beneath the box and independently controlled the frequency and amplitude of the sound waves. The speaker has a diameter of 165 mm and an impedance of 4 Ω. A fibrous spacer ring produces the contact between box and speaker. A sinusoidal audio signal was generated with the software SWEEPGEN v3.7.6. This signal was delivered to the speaker with a 50 W subwoofer amplifier, as illustrated in Fig. 2. The sound level recorded is relative to the maximum volume possible, which is set for reference as a volume of 0 dB.

When put together, the test box rests on a base, with the speaker placed underneath. Strings are tied to the cast and lead to another string that goes around a pulley positioned exactly above the box. This was carefully balanced to ensure that the cast goes up as straight as possible. At a distance of 80 cm from the plexiglass pane, a CMOS camera by LAVISION is positioned in such a way that the viewing direction is perfectly perpendicular to the glass pane. This camera is controlled by the PIV-software DaVis by LAVISION. The complete setup is illustrated in Fig. 3.

Before starting an analog experiment, the test box needs to be filled with the analog material. For that, the box is turned upside down and the glass beads are filled in through the hatch. Then, the bottom is sealed again with an aluminum plate and the box is brought back into its normal position so that the crater cast forms the upper surface. During rotation of the box into its normal position, the glass beads sag down and require replenishing through a small pipe that was drilled into the middle of the cast using a pipette. Acoustic vibration by the speaker compacts the material. To avoid volumetric strain from compaction dominating the experiment, the cast was repeatedly refilled and acoustically vibrated until no more campaction occurred and the cast was filled. During this procedure, the amplitude and frequency of the speaker were set to the same values as would be used later in the experiment.

The typical workflow of conducting an experiment begins with starting the recording in the DaVis software. The camera was set to capture 50 frames per second. The speaker is activated and the cast is pulled up in one swift, but smooth, motion. The fluidization caused by the speaker remains in effect throughout the whole experiment. The flow of analog material is documented by the camera. In order to find a configuration of parameters that results in a properly scaled viscosity, we varied grain size, frequency, and amplitude in consecutive experiments. Three different grain sizes were used, each tested thoroughly with four
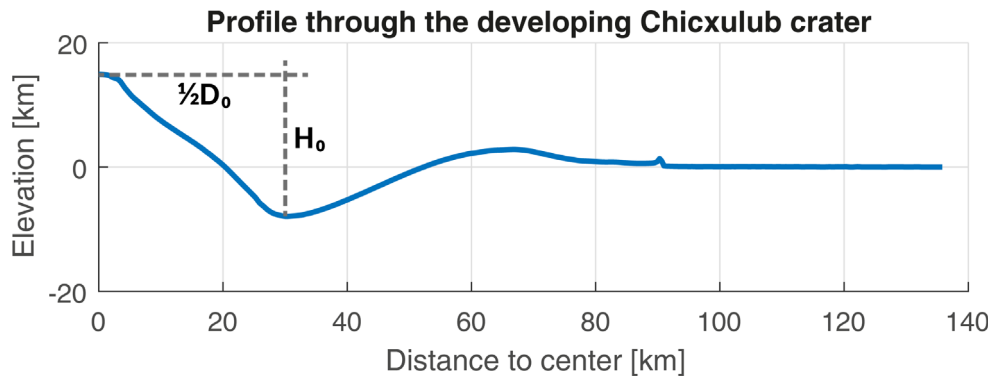
Fig. 2. Profile through the developing Chicxulub crater at the time increment when the central peak has reached the highest extent, taken from a numerical simulation by G.S. Collins (unpublished data). The cast used in our experiments is modeled after this profile. Here, the meaning of the initial diameter, D_0, and height, H_0, of the central peak is illustrated. (Color figure can be viewed at wileyonlinelibrary.com.)
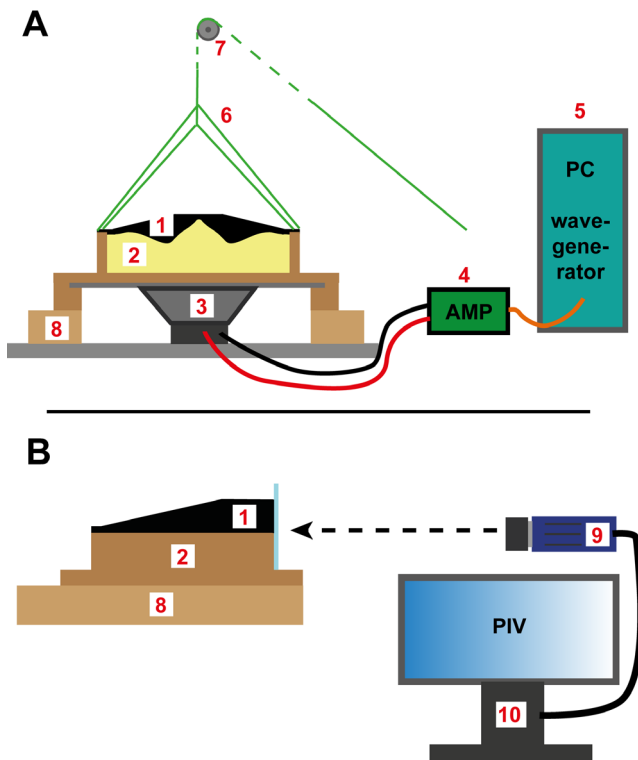

Fig. 3. Schematic illustration of the experimental setup (not to scale). A) Front view. B) Side view. 1) 3-D-printed cast. 2) Containment with glass beads. 3) Subwoofer. 4) Amplifier. 5) PC with audio wave generator. 6) Strings attached to the cast. 7) Pulley. 8) Wooden base. 9) CMOS camera. 10) Computer controlling the camera. (Color figure can be viewed at wileyonlinelibrary.com.)

different frequencies (50, 80, 110, and 140 Hz) and two different amplitudes for each frequency plus experiments without the speaker being active, summing up to a total of 63 experiments. In early tests,

frequencies of 200 Hz and above proved to be very ineffective at fluidizing the material, so the effect of these higher frequencies was not investigated further. Each individual combination of parameters was tested twice.

A morphometric analysis of the obtained structures was conducted using the DaVis software which was calibrated in terms of scale before the experiments. The measurements refer to the 35th frame after the cast completely loses contact with the glass beads (corresponding to 700 ms). We measured (1) the height of the central peak after collapse with respect to the null level (see Fig. 2) and (2) the diameter of the central peak after collapse, defined by the lowest points of the annular trough. These values were normalized by dividing them with the initial values H_0 and D_0, respectively. The normalized ratio of height-to-diameter R_n is

$$R_n = (HD_0)/(H_0D) \tag{7}$$

An SD of the ratio R_n, s, for each pair of experiments with the same parameters was calculated as:

$$s = \sqrt{\frac{1}{n-1}\sum_{i=1}^{n}(x_i - \overline{x})^2} \tag{8}$$

Then, the SDs for the height, diameter, and the ratio of the two were averaged over all 63 evaluated experiments. The mean SD is used as the error.

For the PIV, an open-source software called PIVlab was used (Thielicke and Stamhuis 2014). The settings used for the PIV analysis were the fast-Fourier-transform cross-correlation algorithm (FFT), three to four passes with a decreasing size of the interrogation
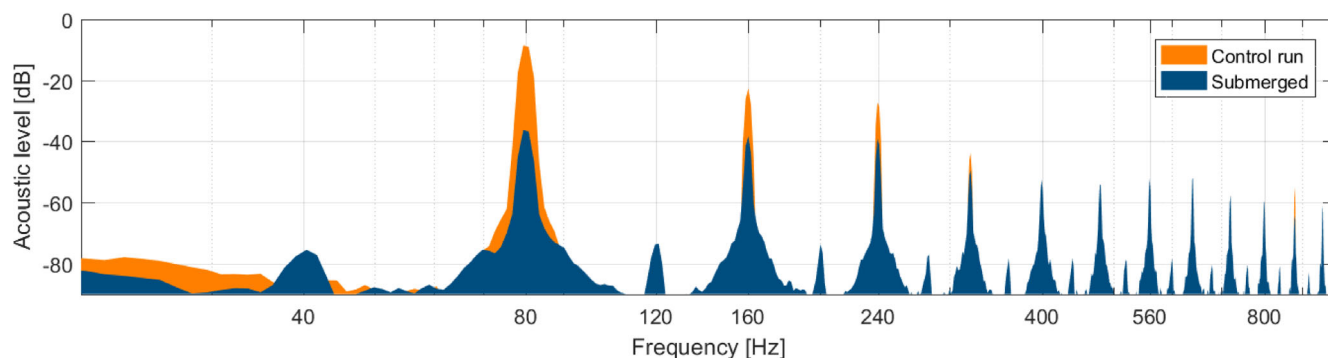
Fig. 4. Frequency spectra from a control run and a recording during which the microphone was submerged in the acoustically agitated medium, both at an input frequency of 80 Hz and a sound level of −10 dB. The peaks show a satisfactory match and an increased contribution of harmonics in the granular medium can be observed. (Color figure can be viewed at wileyonlinelibrary.com.)

window (64–16 px), linear window deformation, and the 2 × 3 gauss subpixel estimator.

To control the acoustic wavelength spectra within the analog material, a separate set of experiments was conducted where a microphone was submerged into the glass beads while the speaker is active. The recorded audio-footage was further analyzed with the software AUDACITY (v2.1.0). For each frequency, a control run was done where the microphone was simply held over the speaker. All showed distinct peaks at the frequency output by the speaker and a few peaks at harmonic frequencies with significantly less intensity (Fig. 4). This confirms that this testing method can be used to accurately measure the frequencies. Some of the control runs showed some noise at frequencies lower than that output by the speaker. The results of measurements where the microphone was submerged in the glass beads and the membrane was in direct contact with the material all had the number and the intensity of the harmonics greatly increased compared to the control runs (Fig. 4). An increased sound level amplified this effect. Generally, the biggest peak remained at the input frequency for the test in the fluidized medium. Little to no noise was detected in these experiments.

A rotational viscometer (PCE-RVI2 (V1R) by PCE instruments) was used to measure the viscosity of the fluidized granular media. The material used for these tests was the 250–420 μm glass beads. Experiments were conducted with three different spindle-speeds, three different frequencies, and two different amplitudes, summing up to a total of 18 experiments. Each measurement lasted three minutes and the measured viscosity was documented every 30 s. After each experiment, the box was emptied and refilled to restore the initial conditions. The amount of glass beads used remained the same throughout all experiments.

RESULTS

The acoustic excitation produced by the subwoofer had a significant influence on the collapse of the central uplift, noticeable both in the shape of the remaining central peak as well as in the kinematics of the collapse as seen by PIV. Acoustic fluidization reduces the height of the remaining central peak and tends to level the morphology (Fig. 5): the top of the central peak is smooth and the slopes are straight, compared to the outcome of an experiment without fluidization. Also, mass movement comes to rest much earlier without fluidization. When processed with PIV, differences in the underlying process are revealed (Fig. 5): without fluidization, the collapse remains an entirely surficial process, the mass movement is restricted to the outermost layer of the central peak in the form of a granular flow. When fluidized, the movement is much more extensive and material deeper inside the central peak is involved. Also, the maximum velocity magnitude achieved is almost three times as high compared to the experiments without fluidization.

Figure 6 shows the analysis of experiment 38. In this experiment, glass beads with a size of 250–420 μm were fluidized at a frequency of 140 Hz and a volume of −15 dB. After removal of the cast, the glass beads are instantaneously released and the strongest movement is located at the tip of the central peak. The top moves downward almost vertically, whereas the material at the upper flanks begins to flow outward and over the slower moving middle section. In the subsequent collapse, growing parts of the flanks become involved in the movement. The material accelerates and reaches a maximum velocity of about 20 mm s^{-1} between 80 and 140 ms after release. At 80 ms, the glass beads begin to move outward and upward onto
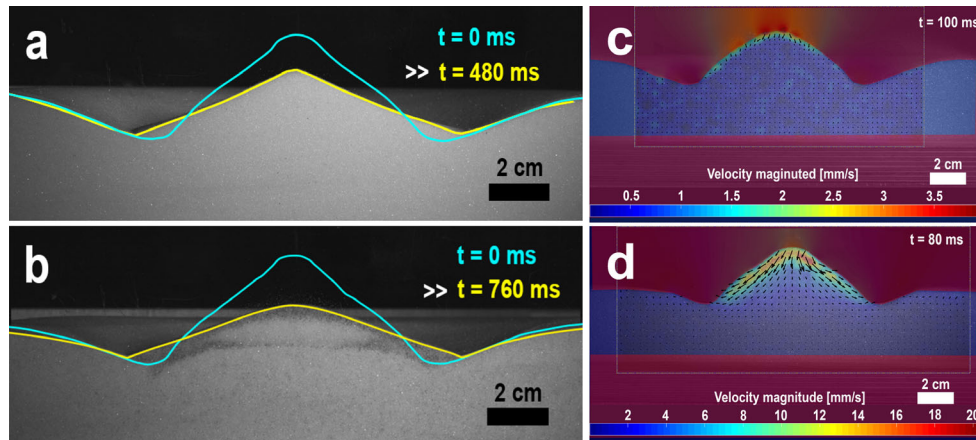
Fig. 5. Pictures (a) and (b) illustrate the resultant morphologies after collapse. a) No fluidization, the peak is pointy, and the slopes are slightly concave. b) Fluidized: rounded peak, straight slopes, overall flatter remaining peak. c and d) Display results of PIV measurements of experiments with and without fluidization: (c) with no fluidization the collapse affects only a shallow layer, while in experiments with acoustic excitation (d) deeper parts of the peak get mobilized.

the slope of the crater wall, as indicated by the vectors at the bottom of the central peak's slopes. Only small amounts of inward movement are detected on the crater walls themselves. From 180 ms on, the rate of deformation declines noticeably and some mostly surficial adjustments of the slope produce the final shape of the collapsed central peak. This is then very slowly altered by a convective flow field as can be seen in the frames (g) and (h) of Fig. 6. The particle trajectories are directed outward and downward with a dominant downward component with respect to the angle of the slopes. The particle velocity in this flow field is much smaller than that of the actual collapse.

The diameter and height of the collapsed central peaks were measured, and a normalized ratio R_n was calculated (Equation 7). This ratio directly reflects the degree of peak collapse: a lower value corresponds to a wider and/or flatter remaining peak. Thus, it is a measure of the influence of the different parameters (grain size, frequency, and volume) on the collapse. If the grain size remains the same, it provides information on the efficiency of a certain frequency or sound level to enhance the collapse. The average of the two experiments done for each unique combination of parameters is displayed in Fig. 7.

The values of R_n are significantly greater for the experiments where the glass beads are not fluidized across all three different grain sizes. This emphasizes the importance of acoustic excitation for material flow. The grain size has a significant, though not simple influence on R_n: the smallest grain size produces the flattest remaining peaks while the intermediate grain size produces the steepest. The coarsest glass beads have R_n

values somewhere in between those of the fine- and medium-sized glass beads (Fig. 7).

The influence of frequency and sound level of the subwoofer on the amount of collapse is not trivial. With a few exceptions, a higher sound level generally produces lower R_n values. While there appears to be a trend toward smaller R_n values for higher frequencies, there are many exceptions and with the available data, the relationship between frequency and R_n remains inconclusive. Two frequencies stand out from the rest: 50 Hz was always the least effective frequency for fluidization of the material, and at the higher amplitude (−10 dB), 80 Hz was the most effective frequency across all grain sizes.

Viscosity Measurements

The viscosities of the fluidized granular media change over time. A linear regression was fitted to the data points (Fig. 8). The first two data points were ignored because the granular medium loses volume when the speaker is turned on. This volume reduction results in the viscometer needing less force to turn the spindle, which results in a reduced viscosity. The average slope is 0.174 Pa for the measurements with 20 rpm and 0.24 Pa for those at 10 rpm. For the subsequent evaluation, the mean viscosity for each test was calculated as the average viscosity of the linear part of each experiment. When the mean viscosities of all tests using the same speaker configuration is plotted against the spindle speed, one can see that the viscosity decreases with increasing spindle speed (Fig. 8). This trend was observed for all three frequencies tested. A
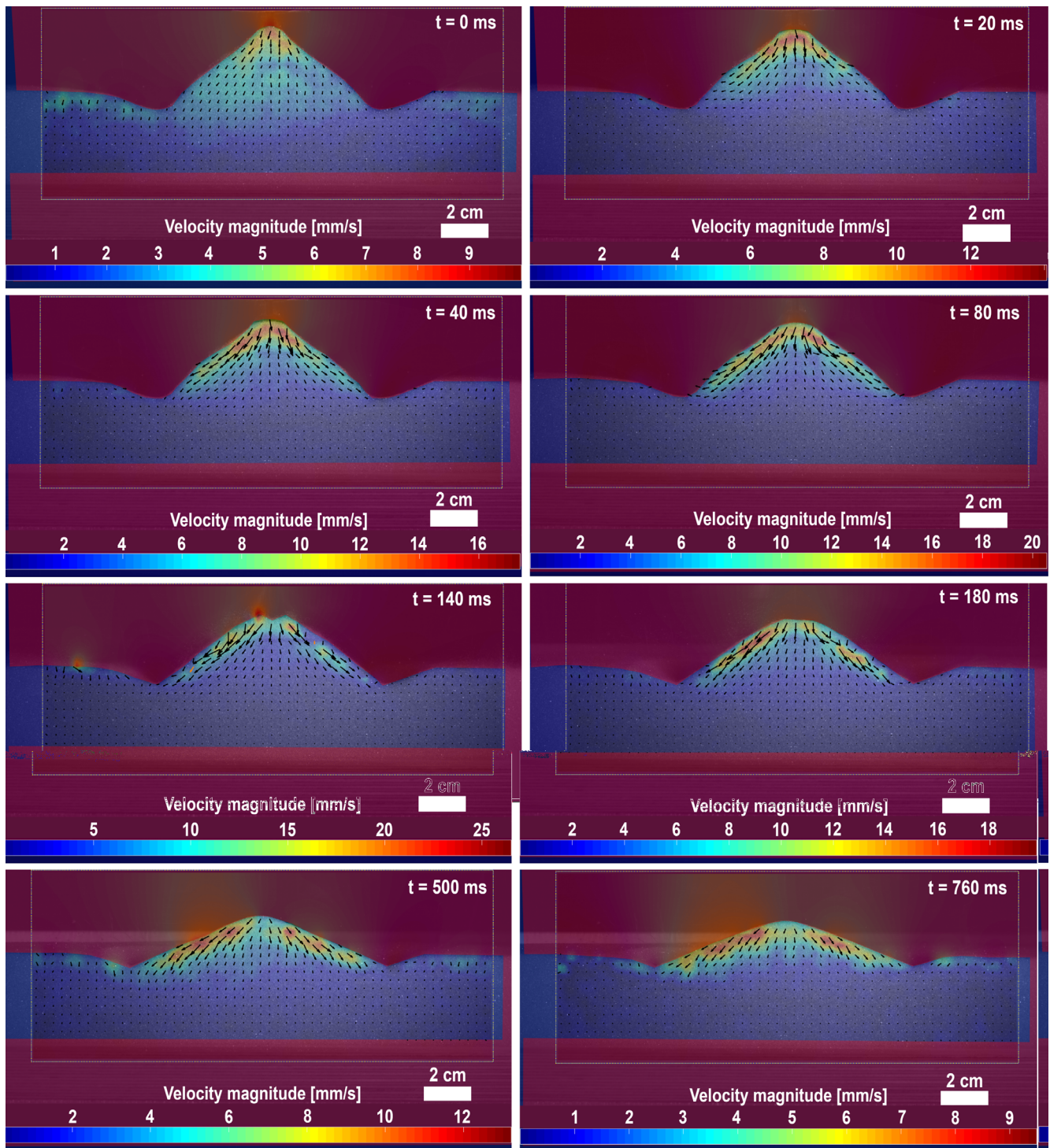
Fig. 6. Crater evolution in experiment 38: the processed footage of experiment 38 (250–420 μm, 140 Hz, −15 dB). Scaling of the color bar is individual for each frame. a–d) At first, the collapse is mostly located at the top, which plunges downward. e, f) Then, the material from the top flows outwards over the slower moving, deeper situated material. From $t = 140$ ms on, the movement is mostly localized at the flanks of the central peak. After the actual collapse has ended, a slow convective flow induced by the speaker remains.
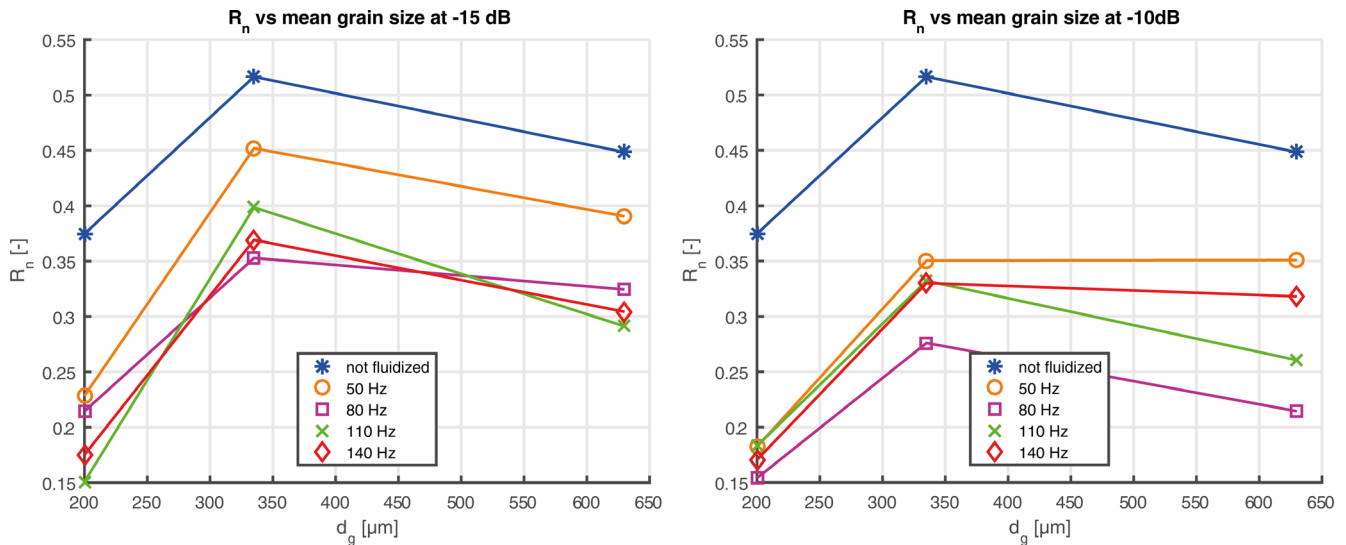
Fig. 7. Results from the morphometric analysis: The grain size d_g shows a clear but nontrivial influence on the effectiveness of the collapse: The smallest grain size produces the flattest and the intermediate grain size the steepest peaks. A higher sound volume almost always results in a more extensive collapse. The effect of the frequency remains inconclusive with 50 Hz being the least effective and 80 Hz at −10 dB the most effective. (Color figure can be viewed at wileyonlinelibrary.com.)

higher sound level resulted in a lower viscosity at all spindle speeds. At constant spindle speed, the viscosity generally decreases with increasing frequency, but the measurements done at 10 and 20 rpm have their minimum viscosity at 80 Hz and show a slight increase at 110 Hz (Fig. 8). At a constant spindle speed, a higher sound level resulted in a lower viscosity for all frequencies. The given error bars are based on an estimated error of measurement from the fluctuations of the viscosity displayed every few seconds.

DISCUSSION

Model Parameters

In our analog experiments, we varied three parameters: the amplitude of acoustic excitation, the frequency of acoustic excitation, and the grain size of the granular material. Although two of these parameters also appear in the block oscillation model—block size and oscillation period—a direct translation of them is not possible. Using Equation 3 and simplifying it to $T = 2\pi\, h/c$ due to the absence of an interbreccia layer in our model, the frequency in the fluidized granular media with average grain sizes of 200–630 µm should range from 5 to 16 kHz, according to the block oscillation model. Assuming a sound velocity of ~200 m s^{-1} in the glass beads (Vriend et al. 2007; Agnolin et al. 2009), the wavelength in the granular material is 1–4 m for frequencies of 50–200 Hz. The average grain size of the largest glass beads would scale to a block size of

370 m in nature. This is similar to the results from Riller et al. (2018), where a 450 m long section of granite in the drill core from the Chicxulub peak-ring might represent a single block. Riller et al. (2018) also offer an alternative interpretation with an average block size of only 3.5 m. Therefore, our analog model cannot serve to directly recreate acoustic fluidization via block oscillation on a laboratory scale. Rather, the variation of the three parameters was done in order to find a configuration of parameters that produce appropriate fluidization and therefore viscosity. When scaled to nature using Equation 5, the viscosity in our experiments would correspond to a viscosity of 4×10^9 Pas in a Chicxulub-sized crater. This is not far from the viscosity used in a recent simulation of the Chicxulub event by Rae et al. (2019a), where an effective viscosity of 2.2×10^9 Pas was used.

Rheology of the Granular Material

The viscosity measurements showed that the fluidized glass beads have a complex non-Newtonian rheology: they exhibit shear-thinning; that is, the viscosity is inversely proportional to the shear rate, which is in agreement with what has been described in several other studies on fluidized granular media. On a grain scale, the mechanism responsible for this is most likely, that at higher shear rates, the increased dilation and reduced contact time between grains inhibit the formation of force chains. The behavior of increasing viscosity with time (rheopexy) can be attributed to the
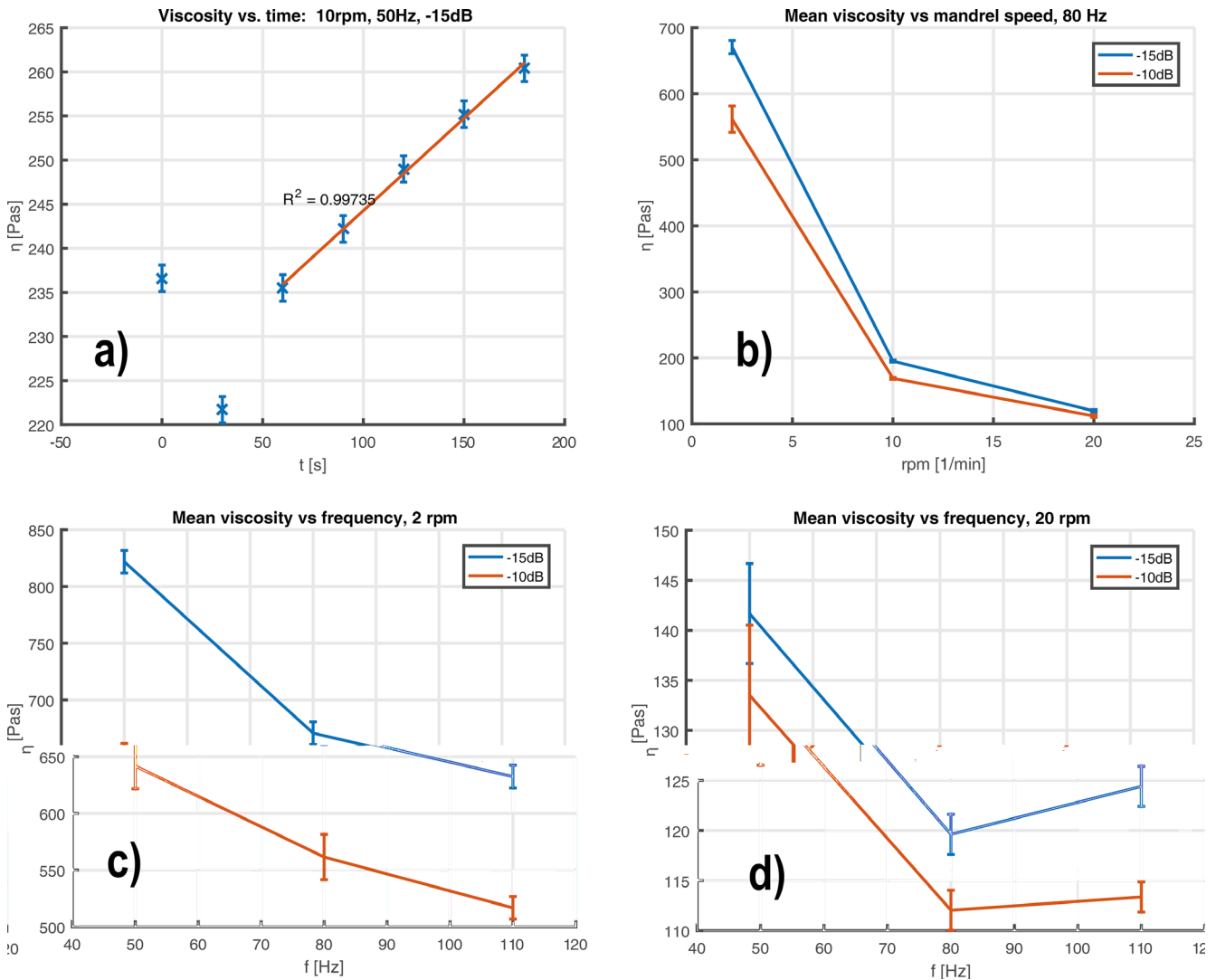
Fig. 8. Results from the viscosity measurements: The viscosity increases with time (a) and decreases with spindle speed (b). There is a trend toward lower viscosities for higher speaker frequencies (c), with a minimum at 80 Hz for some spindle speeds (d). (Color figure can be viewed at wileyonlinelibrary.com.)

compaction of the glass beads facilitated by the vibrations. This effect has also been recognized in previous studies on fluidized granular matter (Marchal et al. 2013; Wortel et al. 2014). Since the volume of the glass beads and thereby the filling height was kept constant during the viscosity measurements, the effect of filling height was not directly investigated. However, the comparatively low mobilization of material deep inside the central peak (Fig. 6d) supports the idea, that the viscosity is inversely proportional to depth, also in accordance with previous observations (Nichol and Van Hecke 2012; Wortel et al. 2014). Furthermore, the initial reduction of viscosity observed at the beginning of each viscosity measurement is also attributed to a loss in volume

and therefore filling height (Fig. 8a). A higher acoustic amplitude always resulted in a lower viscosity. The relationship between frequency and viscosity, however, is less clear: while there seems to be a trend toward lower viscosities at higher frequencies for low shear rates (Fig. 8c), at higher shear rates, there is a viscosity minimum at 80 Hz (Fig. 8d). Taking into account the effect of grain size and using the extent of the collapse given by the measure R_n as a measure of fluidization, the effect of frequency becomes even more inconclusive. Only at the higher amplitude, a frequency of 80 Hz was most effective at fluidizing the material across all grain sizes. According to Xu et al. (2006), the natural frequency n of particle oscillation in a fluidized bed is given by

$$n = \frac{1}{4L} \sqrt{\frac{RT\rho_g}{\varepsilon_b(1-\varepsilon_b)\rho_p}} \qquad (9)$$

where L is the bed height (m), R is the gas constant (286.7 J kg^{-1} K^{-1}), T is the temperature (294 K), ρ_g is the density of air (1.185 kg m^{-3}), ε_b is the bed voidage (–), and ρ_p is the density of the particles. The particle density of the glass beads is 2450 kg m^{-3} (Würth 2017). With this information, the bed voidage can be calculated as:

$$\varepsilon_b = \frac{\rho_p - \rho_b}{\rho_p} \qquad (10)$$

where ρ_b is the bulk density of the glass beads (1500 kg m^{-3}). This results in a bed voidage of 0.39. Using an average bed height L of 0.05 m results in a natural oscillation frequency n of 65.5 Hz. This lies exactly in the middle between 50 Hz, which was arguably the least effective frequency at fluidizing the glass beads and 80 Hz, which seems to be the most effective frequency tested during this study. It should be mentioned that the fluidization accomplished by Xu et al. (2006) was aided by letting gas stream through the bed from below. For further studies, the effectiveness of this supposed natural oscillation frequency should be tested. In a similar setup aimed at producing a fluidized granular target for analog impact experiments, Martellato et al. (2018) found a viscosity minimum in the range of 60–100 Hz for quartz sand and glass beads, respectively. A possible reason for the rather unpredictable influence of frequency on fluidization is resonance effects. The natural frequency spectra of the glass beads are different from the forced vibrations that are applied by the subwoofer. If the forced frequency spectrum is equal or close to the natural frequency, the amplitude of vibration increases manyfold. This phenomenon, known as resonance, would allow neighboring grains to switch their neighborhood more easily and would allow an effective collapse to occur. The natural frequency of the granular target depends on the geometry and dimensions of the experiment box plus cast, which is constant in all experiments, and apparently on grain size. Looking into the effect of the different types of glass beads used, neither grain diameter nor angle of internal friction seems to be the factor governing the extent of uplift collapse (see Fig. 7 and Table 2). Instead, one can see a correlation between the material's cohesion and the resulting values of R_n. If this is not a coincidence, it may be an indication that the central uplift in our model is not fully fluidized and a residual cohesion prevents a more extensive collapse.

Kinematics of Central Uplift Collapse

Similarities and differences between the numerical model of the Chicxulub impact structure (Collins et al. 2002; Morgan et al. 2016) and our analog model were observed. The most obvious difference is that no peak-ring formed in the analog experiments. Instead of a central depression with an elevated ring, a collapsed, broad, and flattened central peak remained as the final product of the collapse in the analog experiments. The resulting morphology is somewhat similar to an intermediate stage of the collapse in the numerical model of a vertical impact (Fig. 9). This may suggest that initially the analog and numerical model behave similarly, but then the collapse in the analog model comes to a halt while the movement continues in the numerical model. Comparing the kinematics of the two models shows that they evolve similarly up to that point. The collapsing central uplift laterally overflows the adjacent annular crater moat, similar to the numerical model and the observation at nature. The general mode of movement as a downward and outward-directed collapse can be identified in both models. However, this movement is differently localized in the two models. In the numerical model of a vertical impact, the central portion of the central uplift collapses straight down while the outer parts of the uplift get pushed outward and thrust upward onto the downfaulted crater walls (Fig. 9). In the analog model, the central top-most volume initially moves downward, and the lower portions begin to move outward onto the crater wall. But then the top portion spreads outward laterally (Fig. 6) without upward thrusting. The flow does not affect the core of the uplift. In an effort to investigate the effects of slope stability on granular slopes, Chou et al. (2013) subjected a triangular pile of granular material to horizontal vibrations. They observed a shallow flow close to the surface at first, followed by a deeper mobilization of the material. This is in contrast to our results, where we see a strong localization of movement at the top of the peak in the beginning, followed by a movement of this material over the lower part of the slope with an additional horizontal component. This shows that although both the collapse of an overheightened central uplift in impact craters and the avalanching in unstable slopes are driven by gravity, they have very distinct kinematics due to the differences of the initial morphology.

There are a number of possible reasons which might have prevented our model to achieve a close match to
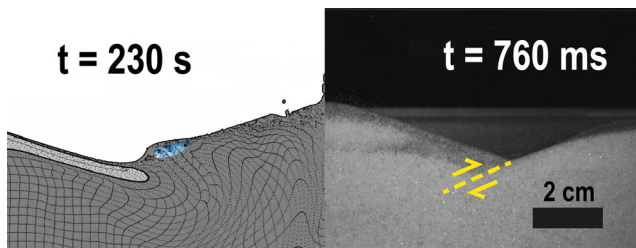
Fig. 9. Juxtaposition of numerical and analog model. The final morphology of the analog model resembles an intermediate stage of collapse in the numerical model (Collins et al. 2002; Morgan et al. 2016). The overthrusting of central-peak material onto the crater walls was also observed in the analog model. (Color figure can be viewed at wileyonlinelibrary. com.)

the kinematics of the numerical simulations or the final peak-ring morphology found in nature.

While the viscosity in the model reasonably matches to that used in Rae et al. (2019a), this viscosity does not necessarily have to be realized in the central peak in the model. Following the practices described by Wortel et al. (2014) and Marchal et al. (2013), and to avoid a rapid volume reduction in the initial stage of collapse, we vibrated the material during the filling of the cast. This, however, might have been detrimental to the subsequent fluidization during the experiment. As described by Wortel et al. (2014) and Marchal et al. (2013), the compaction caused by the vibrations results in a higher viscosity. Furthermore, Umbanhowar and Van Hecke (2005) and Rubin et al. (2006) found that "granular packs are resilient to perturbations up to the maximum perturbation they have previously received." Each granular media has a characteristic critical concentration v_c which is approached during shearing. If the material is overconsolidated its volume increases when sheared, if it is underconsolidated its volume decreases when sheared. Initially, the material in our cast is underconsolidated and very likely the refilling during acoustic excitation causes it to eventually become overconsolidated, hindering a more extensive central peak collapse. The observation that in the analog model, the top of the uplift initially moves straight down and is then deflected outward by the underlying material supports this hypothesis. It is important to point out that this flow field might also be influenced by the plexiglass window that holds back the material.

Finally, inertial effects may hinder the full matching between the analog and numerical models. In the latter, the overshooting of the central uplift and its subsequent collapse that leads to the formation of a peak-ring is a highly dynamic process. Therefore, the assumption of a static starting point as used for the analog model is an

extreme simplification, which might not be able to accurately reproduce the processes taking place in the numerical model and, more importantly, in nature. In the numerical simulation, the crater wall still moves inward when the uplift reaches its highest extent. Also, in the simulation, the collapse does not start simultaneously at all parts of the uplift: the upward movement of the uplift comes to a halt, shortly after the lower flanks have begun to move outward. This initial momentum is lost with the static starting point of the analog model. Furthermore, in the numerical model, there is an equilibrium between the isostatic force driving the upward movement and the gravitational force pulling downward at the moment just before the collapse, which essentially results in a zero-g condition for the rock masses. This is not the case in the analog model, where only the downward force acts on the glass beads.

Moreover, differences between the analog model and numerical modeling can be attributed to inertial forces that cannot be neglected in the experiment. Inertia scales differently with respect to the viscosity. The gravity scaling factor is 1 while that of viscosity is $\sim 10^8$ and mass $\sim 10^{18}$. In the numerical model, inertial forces let material move laterally wider. During the overthrusting of the annular moat, the material piles up to form a peak-ring.

Despite the shortcomings of our analog model, it provides useful insights into the formation of complex craters. Most importantly, our experiments demonstrate that an effective fluidization is necessary for an extensive collapse of the central uplift to occur. Our experiments demonstrate that acoustic excitation is capable of enhancing movement during crater collapse. This study provides independent support for the occurrence of acoustic fluidization during crater modification. The question of how long acoustic fluidization remains active during the formation of complex craters still remains unanswered. Wünnemann and Ivanov (2003) recognized that in numerical simulations implementing the block oscillation model similar results are achieved either by choosing a low viscosity with a short decay time or a higher viscosity with a longer decay time. Recently, Rae et al. (2016) investigated the West Clearwater Lake impact structure using both drill cores and numerical modeling. They raise questions about whether the block model of acoustic fluidization can be used to make accurate predictions about the block size in nature. To achieve a match between their simulations and the observed morphology, they had to use a long decay time, leading them to suggest that regeneration of acoustic waves during uplift collapse occurs. This, however, is not implemented in the block model of acoustic fluidization

(Collins et al. 2002; Rae et al. 2016). Also, Riller et al. (2018) provide an interpretation of their results in which regeneration of the acoustic field alongside with a block size reduction occurs during central uplift collapse.

CONCLUSION

We used a scaled analog material to study the collapse of an acoustically fluidized central peak. A 3-D-printed cast produced from a numerical simulation created the desired starting condition and a subwoofer installed underneath the experiment box generated vibrations, fluidizing the granular material. We investigated the effects of amplitude, frequency, and grain size on the rheology of the fluidized material in order to achieve a properly scaled viscosity. While we see a close match of our scaled viscosity to viscosities used in numerical simulations of the Chicxulub crater formation, our analog model did not result in a peak-ring. Differences between the analog model and numerical model are attributed to scaling problems when comparing inertial forces of model and nature, the static starting conditions of the analog model, and an overconsolidation of the central peak prior to the collapse. Despite these restrictions, we show that the gravitational collapse of an overheightened central peak has fundamentally different kinematics than the avalanching of a simple granular slope, and, more importantly, requires substantial fluidization. This fits with recent studies proposing a regeneration of the acoustic field by the central uplift collapse. The rheological property of shear-thinning makes fluidized granular media a suitable analog material to further investigate this proposed phenomenon. Thus, once the major problem of overconsolidation is addressed —for example, by imposing a stricter control on the volume of refilled glass beads—our new approach toward analog modeling of central uplift collapse provides a way to experimentally verify numerical models and an independent opportunity to study the kinematics of complex crater formation.

Editorial Handling—Dr. Christian Koeberl

REFERENCES

Agnolin I., Roux J.-N., Massaad P., Jia X., and Mills P. 2009. Sound wave velocities in dry and lubricated granular packings: Numerical simulations and experiments. arXiv:0901.2995.

Aschauer J. and Kenkmann T. 2017. Impact cratering on slopes. *Icarus* 290:89–95.

Baker D. M., Head J. W., Fassett C. I., Kadish S. J., and Smith D. E. 2011a. The transition from complex crater to peak-ring basin on the Moon: New observations from the Lunar Orbiter Laser Altimeter (LOLA) instrument. *Icarus* 214:377–393.

Baker D. M., Head J. W., Schon S. C., Ernst C. M., Prockter L. M., Murchie S. L., Denevi B. W., Solomon S. C., and Strom R. G. 2011b. The transition from complex crater to peak ring basin on Mercury: New observations from MESSENGER flyby data and constraints on basin formation models. *Planetary and Space Science* 59:1932–1948.

Baker D. M., Head J. W., Collins G. S., and Potter R. W. 2016. The formation of peak-ring basins: Working hypotheses and path forward in using observations to constrain models of impact-basin formation. *Icarus* 273:146–163.

Barlow N. G. and Bradley T. L. 1990. Martian impact craters: Correlations of ejecta and interior morphologies with diameter, latitude, and terrain. *Icarus* 87:156–179.

Burgert P. 2011. Analogmodellierung zum gravitativen Kollaps instabiler Kraterhohlformen. Diploma, University of Freiburg, Freiburg, Germany.

Campbell C. S. 2005. Granular material flows—An overview. *Powder Technology* 162:208–229.

Childs C., Easton S. J., Vendevill B. C., Jackson M. P. A., Lin S. T., Walsh J. J., and Watterson J. 1993. Kinematic analysis of faults in a physical model of growth faulting above a viscous salt analogue. *Tectonophysics* 228:313–329.

Chou H. T., Lee C. F., and Chen S. C. 2013. The collapse process of granular slopes under seismic forcing. *Earthquake-induced landslides*, edited by Ugai K., Yagi H., and Wakai A. Heidelberg: Springer Verlag. pp. 45–57.

Christeson G. L., Gulick S. P. S., Morgan J. V., Gebhardt C., Kring D. A., Le Ber E., Lofi J., Nixon C., Poelchau M. H., Rae A. S. P., Rebolledo-Vieyra M., Riller U., Schmitt D. R., Wittmann A., Bralower T. J., Chenot E., Claeys P., Cockell C. S., Coolen M. J. L., Ferrière L., Green S., Goto K., Jones H., Lowery C. M., Mellet C., Ocampo-Torres R., Perez-Cruz L., Pickersgill A. E., Rasmussen C., Sato H., Smit J., Tikoo S. M., Tomioka N., Urrutia-Fucugauchi J., Whalen M. T., Xiao L., and Yamaguchi K. E. 2018. Extraordinary rocks from the peak ring of the Chicxulub impact crater: P-wave velocity, density, and porosity measurements from IODP/ICPD Expedition 364. *Earth and Planetary Science Letters* 495:1–11.

Collins G. S., Melosh H. J., Morgan J. V., and Warner M. R. 2002. Hydrocode simulations of chicxulub crater collapse and peak-ring formation. *Icarus* 157:24–33.

Davis D. M., Suppe J., and Dahlen F. A. 1983. Mechanics of fold and thrust belts and accretionary wedges. *Journal of Geophysical Research* 88:1153–1172.

Grant I. 1997. Particle image velocimetry: A review. *Proceedings of the Institution of Mechanical Engineers, Part C: Journal of Mechanical Engineering Science* 211:55–76.

Head J. W. III. 2010. Transition from complex craters to multi-ringed basins on terrestrial planetary bodies: Scale-dependent role of the expanding melt cavity and progressive interaction with the displaced zone. *Geophysical Research Letters* 37:L02203.

Hoth S. 2005. Deformation, erosion and natural resources in continental collision zones. PhD thesis, Freie Universität Berlin, Berlin, Germany.

Ivanov B. A., and Artemieva N. A. 2002. Numerical modeling of the formation of large impact craters. In *Catastrophic events and mass extinctions: Impacts and beyond*, edited by Koeberl C. and MacLeod K. G. Boulder, Colorado: Geological Society of America Special Paper 356:619–630.

Ivanov B. A., and Kostuchenko V. N. 1997. Block oscillation model for impact crater collapse. LPSC abstracts, Vol. 28, p. 631.

Ivanov B. A., Kocharyan G. G., Kostuchenko V. N., Kirjakov A. F., and Pevzner L. A. 1996. Puchezh-Katunki impact crater: Preliminary data on recovered core block structure. LPSC abstracts Vol. 27. pp. 589–590.

Jaeger H. M., Liu C.-H., Nagel S. R., and Witten T. A. 1990. Friction in granular flows. *Europhysics Letters* 11:619–624.

Kenkmann T., and Burgert P. 2011. Impact crater collapse: First experimental results from analogue modeling using particle image strainometry (abstract #1608). 42nd Lunar and Planetary Science Conference. CD-ROM.

Kenkmann T., Ivanov B. A., and Stöffler D. 2000. Identification of ancient impact structures: Low-angle normal faults and related geological features of crater basements. In *Impacts and the Early Earth—Lecture Notes in Earth Sciences 91*, edited by Gilmour I. and Koeberl C. Heidelberg: Springer-Verlag. pp. 271–309.

Kenkmann T., Kiebach F., Rosenau M., Raschke U., Pigowske A., Mittelhaus K., and Eue D. 2007. Coupled effects of impact and orogeny: Is the marine Lockne crater, Sweden, pristine? *Meteoritics & Planetary Science* 42:1995–2012.

Kenkmann T., Collins G. S., and Wünnemann K. 2013. The modification stage of crater formation. In *Impact cratering. Processes and products*, edited by Osinsiki G. R. and Pierazzo E. Oxford: Wiley & Sons. pp. 60–75.

Marchal P., Hanotin C., Michot L. J., and Kiesgen de Richter S. 2013. Two-state model to describe the rheological behavior of vibrated granular matter. *Physical Review E* 88:012207.

Martellato E. and Wünnemann K. 2018. Complex crater formation: Insight from numerical modeling. *Geophysical Research Abstracts 20*, EGU2018-15104. Vienna: EGU General Assembly Vienna.

Martellato E., Wünnemann K., Dörfler M. A., Schuster B., and Kenkmann T. 2018. Experimental investigations of the formation of complex craters. EPSC Abstracts Vol. 12, EPSC2018-96, 2018.

McKinnon W. B. 1978. An Investigation into the role of plastic failure in crater modification. *LPSC abstracts* vol. 9, 3965–3973.

Melosh H. J. 1977. Crater modification by gravity: A mechanical analysis of slumping. In *Impact and explosion cratering*, edited by Roddy D. J., Pepin R. O., and Merrill R. B. New York: Pergamon Press. pp. 1245–1260.

Melosh H. J. 1979. Acoustic fluidization: A new geologic process? *Journal of Geophysical Research: Solid Earth* 84:7513–7520.

Melosh H. J. and Ivanov B. A. 1999. Impact crater collapse. *Annual Review of Earth and Planetary Sciences* 27:385–415.

Morgan J. V., Gulick S. P. S., Bralower T., Chenot E., Christeson G., Claeys P., Cockell C., Collins G. S., Coolen M. J. L., Ferrière L., Gebhardt C., Goto K., Jones H., Kring D. A., Ber E. L., Lo J., Long X., Lowery C., Mellett C., Ocampo-Torres R., Osinski G. R., Perez-Cruz L., Pickersgill A., Poelchau M., Rae A., Rasmussen C., Rebolledo-Vieyra M., Riller U., Sato H., Schmitt D. R., Smit J., Tikoo S., Tomioka N., Urrutia-Fucugauchi J., Whalen M., Wittmann A., Yamaguchi K. E., and Zylberman W. 2016. The formation of peak rings in large impact craters. *Science* 354:878–882.

Nichol K. and Van Hecke M. 2012. Flow-induced agitations create a granular fluid: Effective viscosity and fluctuations. *Physical Review E* 85:061309.

O'Keefe J. D. and Ahrens T. J. 1993. Planetary cratering mechanics. *Journal of Geophysical Research: Planets* 98:17,011–17,028.

O'Keefe J. D. and Ahrens T. J. 1999. Complex craters: Relationship of stratigraphy and rings to impact conditions. *Journal of Geophysical Research: Planets* 104:27,091–27,104.

Phillips R. J., Arvidson R. E., Boyce J. M., Campbell D. B., Guest J. E., Schaber G. G., and Soderblom L. A. 1991. Impact Craters on venus: Initial analysis from Magellan. *Science* 252:288–297.

Rae A. S. P., Collins G. S., Grieve R. A. F., Osinski G. R., and Morgan J. V. 2016. Complex crater formation: Insights from combining observations of shock pressure distribution with numerical models at the West Clearwater Lake impact structure. *Meteoritics & Planetary Science* 52:1330–1350.

Rae A. S. P., Collins G. S., Poelchau M., Riller U., Davison T. M., Grieve R. A. F., Osinski G. R., and Morgan J. V., and IODP-ICDP Expedition Scientists. 2019a. Stress-strain evolution during peak-ring formation: A case study of the chicxulub impact structure. *Journal of Geophysical Research: Planets* 124:396–417.

Rae A. S. P., Collins G. S., Morgan J. V., Salge T., Christeson G. L., Leung J., Lofi J., Gulick S. P. S., Poelchau M., Riller U., Gebhardt C., Grieve R. A. F., and Osinski G. R., and Expedition 364 Sicentists. 2019b. Impact-induced porosity and microfracturing at the Chicxulub impact structure. *Journal of Geophysical Research: Planets* 124:1960–1978.

Riller U., Boutelier D., Schrank C., and Cruden A. R. 2010. Role of kilometer-scale weak circular heterogeneities on upper crustal deformation patterns: Evidence from scaled analogue modeling and the Sudbury Basin, Canada. *Earth and Planetary Science Letters* 297:587–597.

Riller U., Poelchau M. H., mel A. S. P., Schulte F. M., Collins G. S., Melosh H. J., Grieve R. A. F., Morgan J. V., Gulick S. P. S., Lofi J., Diaw A., McCall N., and Kring D. A., and IODP-ICPD Expedition 364 Science Party. 2018. Rock fluidization during peak-ring formation of large impact structures. *Nature* 562:511–518.

Rubin D., Goldenson N., and Voth G. A. 2006. Failure and strengthening of granular slopes under horizontal vibration. *Physical Review E* 74:051307.

Schellart W. P. and Strak V. 2016. A review of analogue modelling of geodynamic processes: Approaches, scaling, materials and quantification, with an application to subduction experiments. *Journal of Geodynamics* 100:7–32.

Swisher N. C. and Utter B. C. 2014. Flow profile of granular avalanches with imposed vertical vibration. *Granular Matter* 16:175–183.

Thielicke W. and Stamhuis E. J. 2014. PIVlab—Towards user-friendly, affordable and accurate digital particle image velocimetry in MATLAB. *Journal of Open Research Software* 2.

Umbanhowar P. and Van Hecke M. 2005. Force dynamics in weakly vibrated granular packings. *Physical Review E* 72:030301.

Vriend N. M., Hunt M. L., Clayton R. W., Brennen C. E., Brantley K. S., and Ruiz-Angulo A. 2007. Solving the mystery of booming sand dunes. *Geophysical Research Letters* 34:L16306.

Wortel G. H., Dijksman J. A., and van Hecke M. 2014. Rheology of weakly vibrated granular media. *Physical Review E* 89:012202.

Wünnemann K. and Ivanov B. A. 2003. Numerical modelling of the impact crater depth-diameter dependence in an acoustically fluidized target. *Planetary and Space Science* 51:831–845.

Würth 2017. Würth Strahlmittel Gesamtübersicht. http://www.eisenwerk-wuerth.de/uploads/media/Firmenprospekt_DE.pdf. Accessed March 17, 2017.

Xu C., Cheng Y., and Zhu J. 2006. Fluidization of fine particles in a sound field and identification of group C/A particles using acoustic waves. *Powder Technology* 161:227–234.